POLITECNICO DI TORINO
Repository ISTITUZIONALE

Numerical Prediction of Internal Flows in He/LOx Seals for Liquid Rocket Engine Cryogenic Turbopumps

Original
Numerical Prediction of Internal Flows in He/LOx Seals for Liquid Rocket Engine Cryogenic Turbopumps / Maritano, Lorenzo; Marin, FRANCESCO MARIA; Bertani, Cristina; Pastrone, Dario Giuseppe; Angelucci, Maddalena; Caggiano, Giuseppe. - In: APPLIED SCIENCES. - ISSN 2076-3417. - 12:21(2022), p. 10776. [10.3390/app122110776]

Availability:
This version is available at: 11583/2972675 since: 2022-10-28T12:35:27Z

Publisher:
MDPI

Published
DOI:10.3390/app122110776

Terms of use:

This article is made available under terms and conditions as specified in the corresponding bibliographic description in the repository

Publisher copyright

(Article begins on next page)

29 March 2024

applied sciences

MDPI

Article

Numerical Prediction of Internal Flows in He/LOx Seals for Liquid Rocket Engine Cryogenic Turbopumps

Lorenzo Maritano [1], Francesco Maria Marin [2], Cristina Bertani [1], Dario Pastrone [1,*], Maddalena Angelucci [2] and Giuseppe Caggiano [2]

[1] Politecnico di Torino, C.so Duca Degli Abruzzi 24, 10129 Torino, Italy
[2] Avio S.p.A., Via I Maggio, 56, 10040 Torino, Italy
* Correspondence: dario.pastrone@polito.it

Abstract: Cryogenic turbopumps are used in high-performance, lightweight liquid rocket engines for space applications. The development of bearings and shaft seals for cryogenic turbopumps requires detailed characterization of the internal flow, taking into account the effects of boiling and multi-component two-phase flow. Here, a flow network solver was developed to analyse the secondary flow circuit of a cryogenic turbopump where the propellant is mixed with high-temperature helium after bearing cooling. The network solver is based on an extension of a classic 1D homogeneous model, originally developed for a pure substance, to the case of two-phase multi-component flow. The solver is capable of predicting pressures, temperatures, flow rates, and species concentrations in a complex two-phase flow in the presence of non-condensable gases. The unsteady mass, momentum, and energy conservation equations are implemented in conjunction with the thermodynamic equations of state using a general-purpose finite volume formulation, where the pressure drop and the heat transfer are calculated using correlations. The numerical tool was validated by comparing its predictions with experimental data obtained during tests on the secondary circuit of an oxygen turbopump developed at Avio S.p.A. A number of engine operating conditions were considered (inlet helium temperature in the range of 250–280 K, helium/liquid oxygen drain in the range of 165–230 K). The predicted temperature values showed good agreement with the experimental data in most conditions.

Keywords: heat transfer; multi-phase flows; boiling; cryogenic propellants; non-condensable gas; homogeneous model; flow network; turbopump; seal package; liquid rocket engine

check for updates

Citation: Maritano, L.; Marin, F.M.; Bertani, C.; Pastrone, D.; Angelucci, M.; Caggiano, G. Numerical Prediction of Internal Flows in He/LOx Seals for Liquid Rocket Engine Cryogenic Turbopumps. *Appl. Sci.* **2022**, *12*, 10776. https://doi.org/10.3390/app122110776

Academic Editors: Andrea Diani and Luca Viscito

Received: 20 September 2022
Accepted: 19 October 2022
Published: 24 October 2022

Publisher's Note: MDPI stays neutral with regard to jurisdictional claims in published maps and institutional affiliations.

Copyright: © 2022 by the authors. Licensee MDPI, Basel, Switzerland. This article is an open access article distributed under the terms and conditions of the Creative Commons Attribution (CC BY) license (https://creativecommons.org/licenses/by/4.0/).

1. Introduction

Cryogenic propellants are rocket propellants stored at very low temperatures. Typically, they are stored in a liquid state at their boiling point. Liquid oxygen (LOx, normal boiling point of 90.2 K), liquid hydrogen (LH2, normal boiling point of 20.3 K), and liquid methane (LCH4, normal boiling point of 111.5 K) are the most commonly used cryogenic propellants [1,2]. Cryogenic solid propellants have also been proposed, but presently, no application exists [3]. On the contrary, propellants such as LOx and LH2 are widely used in space applications due to their excellent performance. High-performance liquid rocket engines can be realized by feeding the engine with high-pressure cryogenic propellants using turbopumps rotating at high shaft speeds. These turbopumps are usually driven by a turbine that is fed by hot gases coming either from a dedicated combustor or from the thrust chamber cooling system. The shaft connecting the turbine to the pump is supported by bearings, which operate at high rotational speeds. The bearings dissipate a large amount of power, thus requiring adequate cooling in order to avoid damage or failure. Due to the low temperatures, conventional lubricants cannot be used, and the only available coolant is the cryogenic propellant itself. Therefore, during engine operation, a small fraction of cryogenic propellant mass flow is redirected towards the bearings using dedicated channels, also called secondary flow systems. Given that the bearing housing is adjacent to the turbine, a

seal system must be incorporated to restrain the leakage of high-pressure cryogenic fluid toward the turbine.

Shaft seals are among the most critical components of a liquid rocket engine turbopump, especially in the oxidizer turbopump, where direct contact between the oxidizer and the hot fuel-rich gases flowing through the turbine must be avoided in all conditions. However, a small leakage of cryogenic fuel toward the fuel-rich turbine gases can be accepted in fuel turbopumps; therefore, the seal system can be simplified in this latter case. In oxidizer turbopumps, a seal package usually provides separation through mechanical barriers (seals, rotating slingers) and by feeding an inert gas such as helium (He) at high pressure between the two fluids. The seal package, therefore, consists of at least three elements: the oxidizer seal, the He purge seal, and the turbine gas seal. The He purge seal is installed between the oxidizer seal and the turbine gas seal and supplies He as a barrier gas. The low temperature of the cryogenic propellants, in combination with the high temperature of the hot turbine gases and the He purge, results in severe temperature gradients through the seal system and across the seal assembly. These thermal gradients determine the thermal deformation of the components, which must be considered when evaluating the seal's clearance.

Several factors must be considered during turbopump design to achieve the required system reliability. One of the main tasks is to accurately predict the pressure and temperature distribution in the secondary flow systems in order to correctly evaluate mass flows through seals and bearings. Modelling the secondary flow paths of a turbopump implies that complex phenomena must be considered. Such a network involves flow through narrow passages between rotating and stationary surfaces, phase changes, fluid mixing, and heat transfer; therefore, two-phase multi-component flows must be modelled. As can also be seen in simpler cases [4–7], the development of appropriate methods is a really challenging task.

Flow network solvers have proven to be the most appropriate tools for the preliminary design and analysis of components and systems involving two-phase heat transfer phenomena. This method simplifies the complex three-dimensional problem by relying on 1D modelling, represented by a series of interconnected elements, which make up the equivalent flow network (nodes linked by branches). The two-phase flow can be predicted by different models, such as the two-fluid model, the drift–flux model, and the homogeneous model [8]. The two-fluid model is the most rigorous approach since each phase is modelled separately with interfacial interactions. Nevertheless, it is rarely applied [9,10] due to the considerable difficulties linked to the uncertainties in predicting the interfacial interaction terms between the two phases and the mathematical complexity of two sets of conservation equations. The drift–flux model provides a simpler and more reliable alternative to the two-fluid models. This model, employed by Wang et al. [11], simulates the behaviour of the two-phase flow as a whole while considering the relative motion between the two phases. In this way, the model uses one set of three conservation equations for the two-phase mixture and a drift–flux equation. The most commonly used approach is the homogeneous model. The model considers the fluid as a homogeneous mixture and employs a set of three conservation equations [12–14]. As an example, this model was adopted by Van Hooser et al. [13] to investigate complex problems such as the chill-down of the feed line with a centrifugal turbopump. They adopted a novel finite-volume-based network flow analysis procedure [14] and demonstrated that fluid networks could be used to simulate geometries as complex as those of a turbopump. It should be noted that fluid network solvers use bulk properties averaged over a cross-sectional area and require a set of correlations based on experimental data [15–24] to accurately determine heat transfer and pressure losses. Therefore, the accuracy of the chosen correlations for the specific application heavily influences the prediction accuracy of the model. Therefore, in order to choose the most suitable correlations, a review of the performance of the different correlations for various fluids and geometries is needed, such as those presented by Kim et al. [25] and Hartwig et al. [7]. Despite its limitations, the homogeneous model for fluid network solvers offers robustness, fast calculations, and good accuracy for preliminary design studies.

Although some research has been carried out on the modelling of the two-phase flow of a pure cryogenic fluid, very little attention has been paid to the role of the mixing of fluid in the presence of phase change.

In a previous work [26], the authors developed a thermo-fluid network solver and used it to simulate a pure substance/two-phase flow in a spinning stator–rotor–stator disk [26]. The purpose of this paper was to improve the aforementioned numerical model by adding the capacity to describe the mixing of different fluids (e.g., oxygen and helium). The numerical tool uses a one-dimensional general-purpose finite volume homogeneous model to predict two-phase multi-component flows in cryogenic feeding systems. A finite difference discretization was employed in the mass, the momentum, and the energy conservation equations of fluids and solids in order to predict thermo-fluid transients during the two-phase flow of cryogenic lines. The classical two-phase heat transfer and pressure drop empirical correlations were adapted to multi-component flows using an overall gas fraction. The numerical model was validated on experimental data collected by Avio S.p.A. during the tests on the Dynamic Seal Package (DSP). A simplified cross-section of the test bench is shown in Figure 1. Experimental data for a number of DSP operating conditions were used as a reference in order to validate the tool and to make it available for the design and analysis of new advanced components.

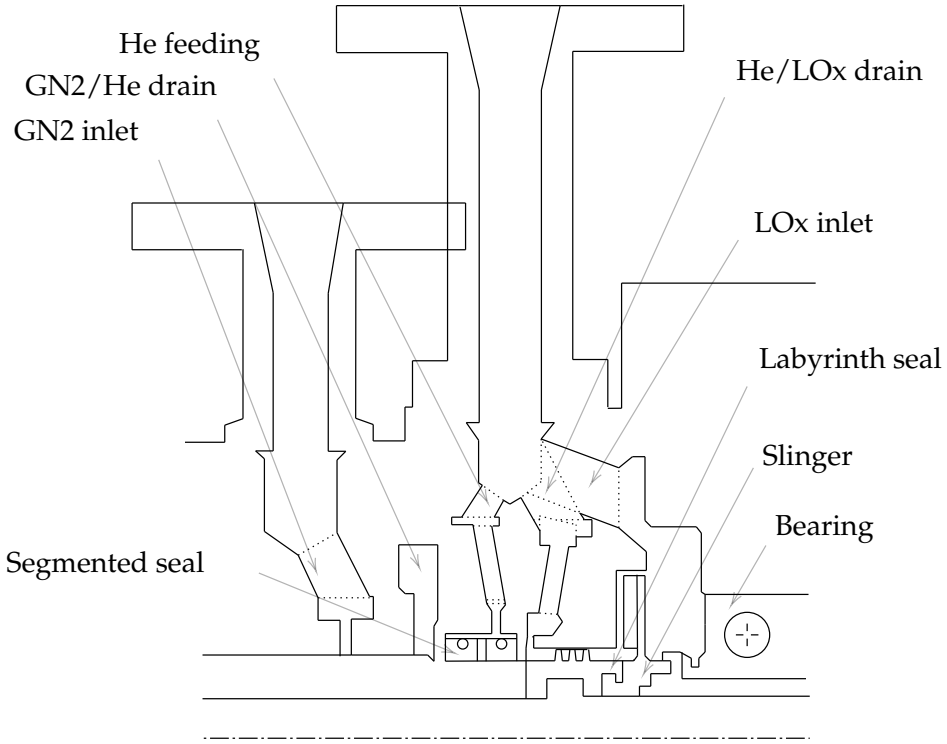


Figure 1. Partial cross-section of the Dynamic Seal Package test bench.

In Section 2, the model assumptions and equations are presented, including the conservation equations, the thermodynamic properties, and the pressure drop and heat transfer correlations. Section 3 presents the test setup and its modelling used in the numerical solver. Section 4 shows the results of the model predictions, highlighting the most relevant properties compared with the experimental data. Finally, Section 5 summarizes the conclusions of the present work.

2. Model Description

Predicting the flow distribution in the flow network requires the solution of unsteady mass, momentum, and energy conservation equations in conjunction with thermodynamic equations of state. The Majumdar approach was adopted [14], involving a general-purpose

finite volume formulation. This formulation was already described in [13,14,26]; therefore, only its most essential features are hereby summarized, together with the new additional equations and correlations needed to describe the mixing of different fluids and the pressure losses through the flow network.

The approach requires a one-dimensional modelling of the analysed system using a network of solid and fluid nodes. The network is characterized by nodes and branches, which can be internal or boundary elements (see Figure 2). The fluid path was partitioned into a discrete number of control volumes, and the conservation equations for each control volume were solved. At the boundary branches, flow rates were imposed with the input fluid's temperature, pressure, and species concentration, while only pressure is defined at the boundary nodes. Pressures, temperatures, flow rates, and species concentrations were determined by solving the time-dependent mass and energy conservation equations at the internal nodes, in conjunction with the thermodynamic equation of state and the time-dependent momentum conservation equation, in all internal branches. The walls were discretized in the same manner, creating a network of solid nodes. The temperatures were computed by solving a solid time-dependent energy conservation equation for each solid node together with the conduction and convective heat transfer determined in each solid-to-solid and solid-to-fluid branch.

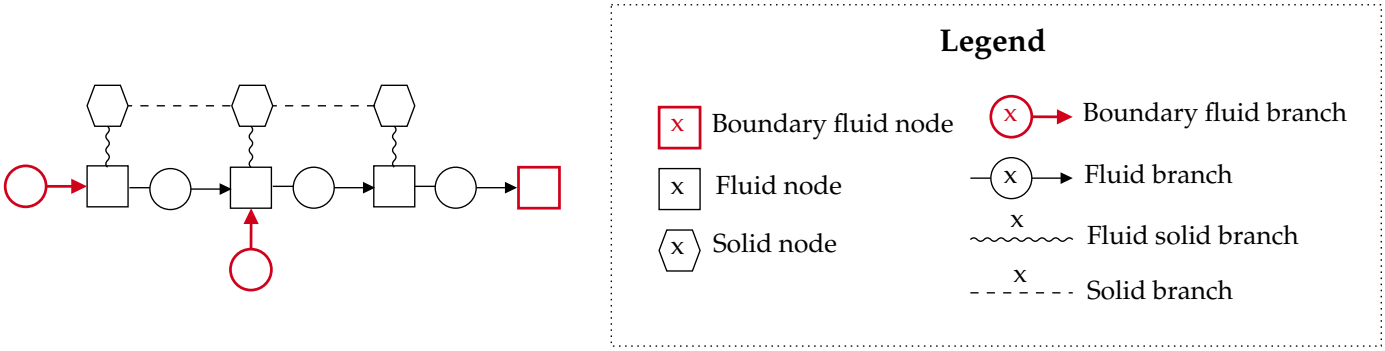


Figure 2. Example of the schematization of a simple system into nodes and branches with indexing practice.

2.1. Mass Conservation Equations

For the transient formulation, the mass conservation equation requires that the net mass flow rates entering a given node be equal to the rate of change of mass in that control volume. In the presence of a mixture, the species mass fraction must be computed to determine the fluid properties accurately. Here, a modified formulation of the mass conservation proposed by Majumdar [14] was used. For the k^{th} species at fluid node i, the equation adopted is:

$$\frac{(m_{i,k})_{t+\Delta t} - (m_{i,k})_t}{\Delta t} = \sum_{j}^{n_{\text{fn}_i}} \left(\beta_{j,k}\, \dot{m}_{ji} - \beta_{i,k}\, \dot{m}_{ij} \right) \tag{1}$$

where $\dot{m}_{ji}$ and $\dot{m}_{ji}$ are the inlet and outlet mass flow rates from the i^{th} node. β_k is the species mass fraction and can be expressed as a function of the resident mass in the control volume, $\beta_k = (m_k)/(\sum_{k=1}^{n_s} m_k)$.

2.2. Momentum Conservation Equations

The mass flow rate in a fluid branch was calculated from the balance of fluid forces on a given branch, involving the momentum conservation equation [14]:

$$\begin{aligned} &\frac{(m_{ij}\, u_{ij})_{t+\Delta t} - (m_{ij}\, u_{ij})_t}{\Delta t} + \dot{m}_{ij}\left(u_{ij} - u_{\text{u}}\right) = \\ &\left(p_i - p_j\right) A_{ij} + \rho g V_{ij} \cos\theta - \Delta p_{\text{f}} + \rho K_{\text{rot}}^2 \omega^2 A \end{aligned} \tag{2}$$

where the velocity is determined from the mass flow rate and the branch density, $u = \frac{\dot{m}}{\rho_{ij} A_{ij}}$. The fluid's inertia is represented by the two terms on the left side of the equation. The first term is the time-dependent term required for the transient formulation. The second term is relevant only for significant variations in area or density from branch to branch. On the right side of the equation, the forces linked to the pressure gradient in the branch and the effect of gravity, friction, and the centrifugal force (present only when the branch is rotating) are considered, respectively. Regarding the test case used to validate the model, the fluid density and the differences in height are relatively low. Therefore, it is possible to assume that the gravitational force term in the momentum conservation equation can be neglected.

2.3. Energy Conservation Equations of Fluid

The energy conservation equation at fluid node i can be expressed in terms of enthalpy as [14]:

$$\frac{m_i\left(h_i - \frac{p_i}{\rho_i}\right)_{t+\Delta t} - m_i\left(h_i - \frac{p_i}{\rho_i}\right)_t}{\Delta t} = \sum_j^{n_{\mathrm{fn}_i}} \left(h_j \dot{m}_{ji} - h_i \dot{m}_{ij}\right) - \dot{Q}_{\mathrm{fs},i} \tag{3}$$

where $\dot{Q}_{\mathrm{sf}}$ is the heat transfer from the connected solid nodes and can be expressed for the i^{th} node as $\dot{Q}_{\mathrm{sf},i} = \sum_j^{n_{\mathrm{sn}_i}} \dot{Q}_{ji_{\mathrm{fs}}}$.

2.4. Energy Conservation Equations of Solid

When considering heat transfer with the wall, it is also necessary to adopt an additional energy conservation equation formulated for the solid elements of the network to estimate the wall temperature. For the i^{th} solid node, the rate of change in the temperature of the node must equal the power exchanged with the adjacent solid and fluid nodes. Therefore, the equation can be expressed as:

$$\frac{m_i\, \bar{c}_{\mathrm{p},i}\left((T_{\mathrm{s},i})_t - (T_{\mathrm{s},i})_{t+\Delta t}\right)}{\Delta t} = \dot{Q}_{\mathrm{ss},i} + \dot{Q}_{\mathrm{fs},i} \tag{4}$$

where $\dot{Q}_{\mathrm{fs},i} = \sum_j^{n_{\mathrm{fn}_i}} \dot{Q}_{ji_{\mathrm{fs}}}$ and $\dot{Q}_{\mathrm{ss},i} = \sum_j^{n_{\mathrm{sn}_i}} \dot{Q}_{ji_{\mathrm{ss}}}$. In this equation, $\bar{c}_{\mathrm{p},i}$ is the mean specific heat of the i^{th} solid node and is computed as $\bar{c}_{\mathrm{p},i} = \frac{(c_{\mathrm{p},i})_t + (c_{\mathrm{p},i})_{t+\Delta t}}{2}$.

2.5. Heat Transfer Model

The fluid–solid and solid–solid heat transfer coefficients are necessary to calculate the heat transfer terms involved in the energy conservation equations. For a generic fluid-to-solid and solid-to-solid branch, the power exchanged between nodes can be expressed as:

$$\dot{Q}_{\mathrm{fs}} = h_{\mathrm{fs}}\, \Delta T_{\mathrm{fs}}\, A_{\mathrm{fs}} \tag{5}$$

$$\dot{Q}_{\mathrm{ss}} = h_{\mathrm{ss}}\, \Delta T_{\mathrm{ss}}\, A_{\mathrm{ss}} \tag{6}$$

2.5.1. Fluid–Solid Heat Transfer

The cryogenic fluid encounters a wide range of flow conditions during a cooling process. The resulting complex heat transfer regimes imply that the modelling of the convective heat transfer requires multiple correlations for each flow regime. Reference is made to the classical subdivision of two-phase flow regimes: single-phase gas flow, dispersed flow, annular flow, transition flow, bubbly flow, and single-phase liquid flow; see Figure 3.

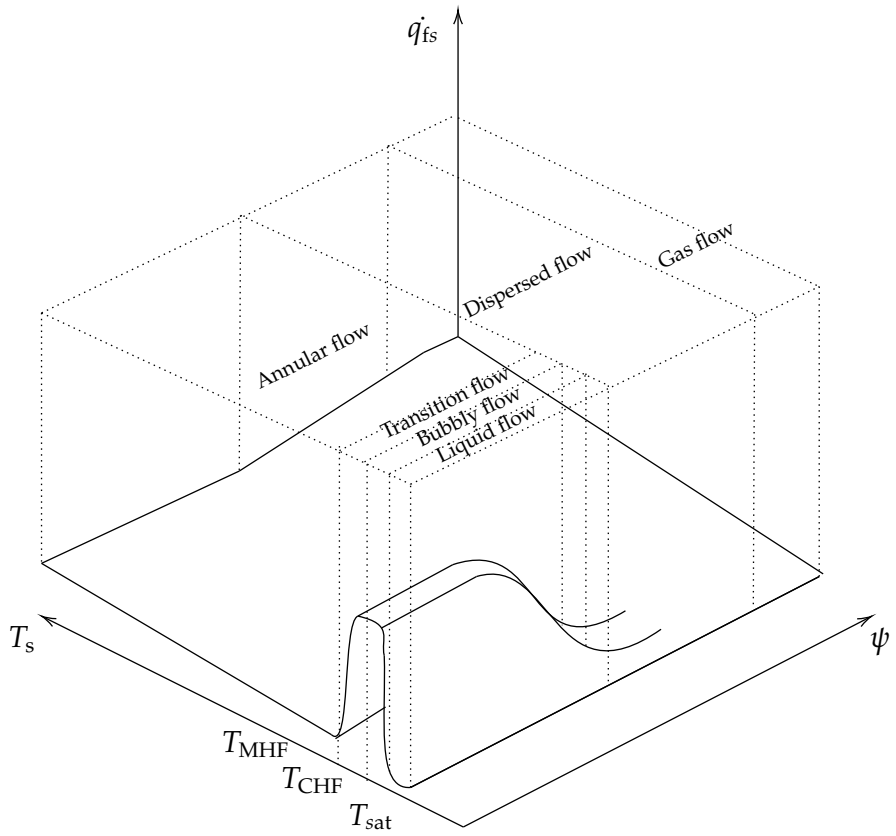


Figure 3. Heat flux variation vs. temperature and overall gas fraction.

The popular Dittus–Boelter correlation [27,28] was used in this model to calculate the heat transfer coefficient for *single-phase liquid or gas flows*:

$$h_{sp} = 0.023 \frac{k}{D_h} Re^{0.8} Pr^{0.4} \tag{7}$$

with $Re = \frac{G D_h}{\mu}$, $Pr = \frac{\mu c_p}{k}$, and $G = \frac{\dot{m}}{A}$.

In the case of film boiling, the fluid can present two different flow regimes: *dispersed flow* and *annular flow*. In the dispersed flow regime, the gas fraction is relatively high. The gas flows as a continuous phase in the pipe, and the liquid phase is present as dispersed droplets in the gas core. As the gas fraction reduces, a liquid film appears on the pipe walls, while the core of the pipe is still occupied by gas and liquid droplets. Several correlations are available in the literature to calculate the heat transfer coefficient in these regimes. For the liquid-deficient dispersed film boiling regime, we adopted the approach of Dougall-Rohsenow et al. [29], modifying it to take into account the presence of an incondensable phase:

$$h_{disp} = 0.023 \frac{k_v}{D_h} \left\{ Re_v \left[\psi + \frac{\rho_v}{\rho_l} (1 - \psi) \right] \right\}^{0.8} Pr_v^{0.4} \tag{8}$$

In contrast with the original correlation, here, ψ is the overall gas fraction, expressed as $\psi = \sum_{k=1}^{n_s} \psi_k \beta_k$ for the generic case of a mixture. The gas fraction for the component k^{th}, ψ_k, is $\psi_k = 1$ in the case of inert gas (He), while $\psi_k = x_k = (h - h_{sat})/h_{lv}$ for the two-phase fluid (oxygen). For the annular film boiling, the Bromley-type relation [30,31] modified by Li et al. [12] was applied:

$$h_{annular} = 0.673 \left\{ \left[\frac{\sigma}{(\rho_l - \rho_v) g} \right]^{0.5} 2\pi \right\}^{-0.25} \left[\frac{g \rho_v (\rho_l - \rho_v) h'_{lv} k_g^3}{\mu_v (T - T_{sat})} \right]^{0.25} \left(\frac{u}{0.076} \right)^{0.5} \tag{9}$$

where h'_{lv}, the equivalent latent heat including the effect of vapour superheat, is expressed as $h'_{lv} = h_{lv} + 0.4\,(T - T_{sat})\,c_{p,v}$.

Finally, at an even lower gas fraction, *bubbly flow* and *transition flow* occur: bubbles flow through a continuous liquid phase. For these two flow regimes, the heat flux is estimated by interpolating between the liquid single-phase and the critical and the annular heat flux as a function of the wall temperature. For the critical heat flux, the Jin et al. correlation [20] was adopted to give encouraging results:

$$\dot{q}_{CHF} = 6.08 \cdot 10^{-3} h_{lv}\, G \left(\frac{\sigma\, \rho_l}{G^2\, D_h} \right)^{-0.268} \tag{10}$$

This correlation was derived from the Katto and Kurata relation and was obtained from experimental data of chill-down processes on LN_2, LAr and LO_2 conducted by Jin. It returned a prediction of good accuracy, with a mean absolute error of 20%.

As shown by Figures 3 and 4, the correlations for the heat transfer coefficient, h_{fs}, were selected according to the flow regimes. The flow regimes in two-phase conditions were determined by comparing the fluid temperature, T, with the critical and minimum heat flux temperatures, T_{CHF} and T_{MHF}, and as a function of the overall gas fraction, ψ. The minimum heat flux temperature, or rewet temperature, is the temperature that signals the end of film boiling and is determined by the correlation proposed by Darr et al. [32]. On the other hand, the critical heat flux temperature is the temperature associated with the maximum heat flux and is evaluated by adopting Kalinin's correlation [33], adapted with the new formulation for T_{MHF}.

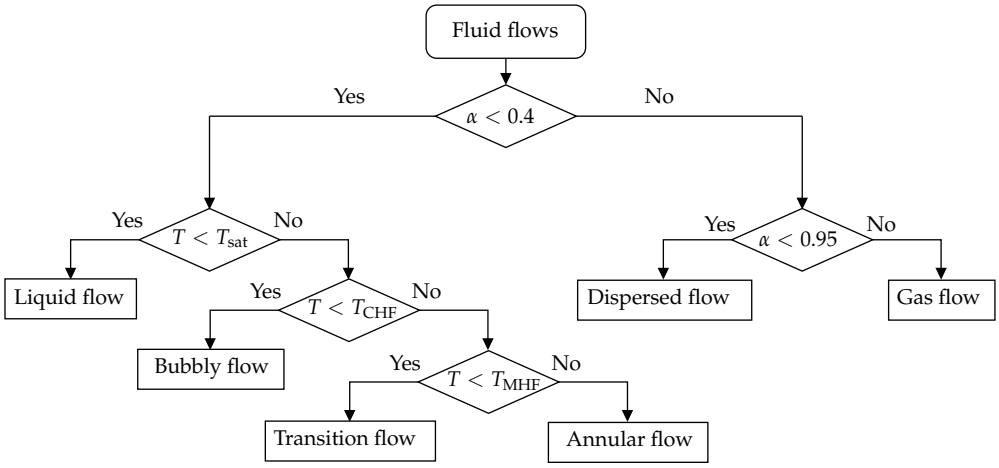


Figure 4. Flow regimes' identification chart.

2.5.2. Solid–Solid Heat Transfer

Unlike fluid–solid heat transfer, heat transfer within a solid can be accurately estimated from the thermal conductivity of the wall material without the use of correlations:

$$h_{ss} = \frac{k_s}{\delta} \tag{11}$$

where k_s can be estimated from the the solid temperature.

2.6. Pressure Losses Model

The pressure losses are the most relevant terms to consider in the momentum conservation equation. These terms can be modelled as the sum of two contributions: one related to the friction along the conduit (alias line pressure drops) and the other related to the local pressure losses due to pipe fittings and changes in stream direction.

$$\Delta p_f = \Delta p_l + \Delta p_k \tag{12}$$

To estimate the contributions in the friction term, empirical correlations are required.

2.6.1. Line Pressure Drop

The present model considers different relations for the line pressure drop depending on the fluid flow regime. The line pressure drop is evaluated as

$$\Delta p_{\mathrm{l}} = \frac{dp}{dz} L \tag{13}$$

For the *single-phase regime*, the Colebrook correlation was adopted [34]:

$$\begin{cases} \left(\frac{dp}{dz}\right)_{\mathrm{sp}} = \frac{2G^2}{\rho D_{\mathrm{h}}} f \\ \frac{1}{\sqrt{f}} = -2 \log\left(\frac{\varepsilon}{3.7 D_{\mathrm{h}}} + \frac{2.51}{Re\sqrt{f}}\right) \end{cases} \tag{14}$$

Like the Blasius and the von Karman–Nikuradse relations, this correlation is commonly used for fluids at high saturation temperatures. However, later studies conducted by Zhang et al. [35,36] and Zhong et al. [37] verified that these equations predict pressure losses with single-phase cryogenic fluids with good accuracy. The advantage of using the Colebrook correlation lies in its accuracy, even for small-diameter ducts.

For the *two-phase regime*, numerous correlations have been formulated in the literature to estimate the pressure drop of straight ducts. Several studies, such as those of Kim and Mudawar [25], Yun and Jeong [38], Zhang et al. [39], and Chen et al. [40,41], compared the many available relationships with data for different cryogenic fluids and duct diameters. Analyses of these reviews showed that the Friedel [42] and the Müller-Steinhagen and Hack [43] correlations have the highest overall accuracy and appear to be the most suitable for use within a computational code, at least for larger pipelines. Therefore, in this context, the Müller-Steinhagen and Hack correlation was adopted:

$$\left(\frac{dp}{dz}\right)_{\mathrm{tp}} = \left\{\left(\frac{dp}{dz}\right)_{\mathrm{sp,l}} + 2\left[\left(\frac{dp}{dz}\right)_{\mathrm{sp,v}} - \left(\frac{dp}{dz}\right)_{\mathrm{sp,l}}\right]\psi\right\}(1-\psi)^{1/3} + \left(\frac{dp}{dz}\right)_{\mathrm{sp,v}}\psi^3 \tag{15}$$

where $\left(\frac{dp}{dz}\right)_{\mathrm{sp,l}}$ and $\left(\frac{dp}{dz}\right)_{\mathrm{sp,v}}$ are the pressure gradients, determined by the single-phase correlation assuming the saturated liquid and saturated vapour properties.

2.6.2. Local Pressure Drop

Finally, for all those networks involving an articulated geometry, the pressure drop across fittings and valves must be calculated to accurately estimate the friction term in the momentum conservation equation. In this model, the local pressure drop was formulated following the experimental correlations defined by Idelchik [44], which allow the calculations of the pressure drop for different fittings and values as a function of mass flow and geometry. For a complete discussion on the topic, the reader is recommended to read the reference.

2.7. Thermodynamic Properties and Equation of State

The thermodynamic and thermo-physical properties of the fluid need to be calculated when solving the conservation equations. The properties of the fluid in a given node

were computed from its pressure and enthalpy using available libraries that calculate the properties of the most common pure fluid.

$$\begin{cases} T_k = f(h_k, p) \\ \rho_k = f(h_k, p) \\ c_{p,k} = f(h_k, p) \\ \mu_k = f(h_k, p) \\ k_k = f(h_k, p) \end{cases} \tag{16}$$

In this context, we adopted *CoolProp* [45], a C++ library that implements pure and pseudo-pure fluid equations of state and transport properties for 122 components. The equations of state used in CoolProp are based on Helmholtz energy formulations and can predict the fluid's properties in the different states in which it can exist: subcooled liquid, saturated liquid, vapour, saturated vapour, and superheated vapour.

In the presence of a mixture, additional equations must be considered to evaluate the enthalpy associated with each species and then estimate the thermodynamic properties of the fluid. Following the assumptions of a homogeneous model, the distribution of enthalpy in the species can be determined iteratively from the enthalpy and mass fraction of the mixture by performing an energy balance and imposing an equal temperature between the components of the mixture in the control volume:

$$\begin{cases} T_{i,k}(h_{i,k}, p_i) = T_{i,k+1}(h_{i,k+1}, p_i) \qquad \text{with} \quad k = 1, 2, \ldots, n_s - 1 \\ \sum_{k=1}^{k=n_s} \beta_{i,k}\, h_{i,k} = h_i \end{cases} \tag{17}$$

The properties of a homogeneous mixture of multiple species can be modelled from the properties of the component species. As shown in Equation (18), the density was estimated in this context using Amagat's Law of Partial Volumes, while the other properties were calculated as the molar averages of the component properties.

$$\begin{cases} \frac{1}{\rho} = \sum_{k=1}^{k=n_s} \frac{\beta_k}{\rho_k} \\ c_p = \sum_{k=1}^{k=n_s} \chi_k\, c_{p,k} \\ \mu = \sum_{k=1}^{k=n_s} \chi_k\, \mu_k \\ k = \sum_{k=1}^{k=n_s} \chi_k\, k_k \end{cases} \tag{18}$$

Finally, the state equation was adopted to compute the pressure in the control volume implicitly. For the ith fluid node, the mass can be expressed as:

$$m_i = \rho_i\, V_i \tag{19}$$

where the fluid density, ρ, is a function of the fluid's enthalpy, mass fraction, and pressure in the control volume and the resident mass is calculated from the mass conservation equations.

2.8. Nonlinear Solver

The equations described in the previous sections are necessary to compute the variables of interest of a given thermo-fluid network. The governing equations can be written as $\mathbf{F}(\mathbf{x}) = 0$, where $\mathbf{x}$ is the n-dimensional state array containing the unknown resident masses, wall temperature, pressure, flow rate, and species enthalpies. The function $\mathbf{F} : R^n \rightarrow R^n$ represents the discrete governing equations. The mathematical closure is shown in Table 1, which lists each variable and the designed governing equation to solve that variable.

Table 1. Mathematical closure of the model formulation, where each state variable and the designed governing equation to solve that variable are listed.

State Variable	Governing Equation
Species masses	Mass conservation equations (Equation (1))
Flow rate	Momentum conservation equations (Equation (2))
Fluid enthalpy	Energy conservation equations of fluid (Equation (3))
Species enthalpies	Energy equations of fluid (Equation (17))
Wall temperature	Energy conservation equations of solid (Equation (4))
Pressure	Thermodynamic state (Equation (19))

The simplest iterative procedures for solving a nonlinear algebraic system of equations use the successive substitution method and Newton's method [46]. One of the drawbacks of using Newton's method is the CPU computational cost related to the evaluation of the Jacobian matrix each iteration. Therefore, Broyden's method was employed to solve the discrete nonlinear system [47]. This method was chosen because it is a powerful alternative to Newton's, capable of reducing the amount of calculation at each iteration without significantly degrading the convergence speed. The idea behind the Newton method for solving nonlinear equations, $f(x) = 0$, is to start from an initial guess, x_n, and then approximate the function by its tangent line. The root of this line, x_{n+1}, is the new approximation of the solution and is typically a better estimation of the previous guess. Therefore, by iterating the procedure, it is possible to find a good estimation of the solution. In multiple dimensions, the approach can be summarized as follows:

$$\mathbf{x}_{n+1} = \mathbf{x}_n - \mathbf{J}^{-1}(\mathbf{x}_n)\,\mathbf{F}(\mathbf{x}_n) \tag{20}$$

where $\mathbf{J}(\mathbf{x}_n)$ is the Jacobian matrix evaluated in $\mathbf{x}_n$. Broyden's method generalizes the idea behind the secant method to approximate the derivative by a finite difference and gives a systems generalization of this approach:

$$\mathbf{J}(\mathbf{x}_{n+1}) \approx \frac{\mathbf{F}(\mathbf{x}_{n+1}) - \mathbf{F}(\mathbf{x}_n)}{\mathbf{x}_{n+1} - \mathbf{x}_n} \tag{21}$$

The idea behind this method is to compute the whole Jacobian only at the first iteration and to perform rank-one updates at all other iterations.

$$\mathbf{J}(\mathbf{x}_{n+1}) \approx \mathbf{J}(\mathbf{x}_n) + \frac{\Delta\mathbf{F}_n - \mathbf{J}(\mathbf{x}_n)\,\Delta\mathbf{x}_n}{\Delta\mathbf{x}_n^\top\,\Delta\mathbf{x}_n}\,\Delta\mathbf{x}_n^\top \tag{22}$$

with $\Delta\mathbf{x}_n = \mathbf{x}_{n+1} - \mathbf{x}_n$ and $\Delta\mathbf{F}_n = \mathbf{F}(\mathbf{x}_{n+1}) - \mathbf{F}(\mathbf{x}_n)$. In this way, the approximate Jacobian matrix's inverse is directly determined at each iteration, reducing the arithmetic operation from $\mathcal{O}(n^3)$ to $\mathcal{O}(n^2)$.

For complex networks, the application of this method may be much more convenient in terms of CPU computational cost, as the dimension of the system, n, is proportional to the number of elements and species in the network, $n = n_{\text{ifn}}\,n_{\text{s}} + 2\,n_{\text{ifn}} + (n_{\text{s}} - 1)\,n_{\text{ifn}} + n_{\text{fb}} + n_{\text{sn}}$.

3. Dynamic Seal Package

As previously stated, the test bench for the DSP components developed by Avio was taken as a reference application. A redesigned and more compact DSP dedicated to a new oxygen turbopump was tested to verify the separation between the hot gases feeding the turbine (+600 °C) and the LOx on the pump side (−180 °C). A dedicated test bench was therefore developed to simulate the oxidizer turbopump's secondary flow paths and test the DSP's operation.

Figure 4 shows a simplified cross-section of the DSP test bench. The assembly was characterized by the oxidizer turbopump's shaft, the bearings, the seal package, and a

series of inlet and drainage ducts used to simulate the inlets and outlets of fluids within the secondary flow paths. The DSP uses He as a buffer fluid and keeps the internal fuel and oxidizer seal leakage flows separated. The gaseous nitrogen (GN2) and LOx inlets are two conduits that simulate the hot gas from the turbine and the oxidizer flow used to cool the bearings, respectively. He is injected between the two fluids through the He inlet at a pressure high enough to guarantee no flow return across the segmented seal, avoiding mixing between the two propellants. Both GN2 and LOx mix with He in two separate drainage ducts and exit the assembly. Finally, the slinger and the labyrinth seal were designed to lower the pressure and density of the oxygen flowing from the bearing's chamber to the drainage, thus limiting the oxygen leakage.

The validation of the numerical tool was carried out considering the portion of the Dynamic Seal Package dedicated to He/LOx. The DSP test bench is instrumented with several probes to check the operation of the DSP under various conditions. Four temperature probes were selected to carry out the validation of the tool, two of which are located in the drain conduit, while the other two are in the He inlet. Both pairs of probes are placed radially opposite each other in the outer crown, aligned with the drainage conduit.

3.1. DSP Model

The geometry of interest was divided into control volumes linked to the network nodes and branches. In Figure 5, a transversal cross-section of the He/LOx drain and He inlet of the DSP test bench is reported in order to show the nodes and branches' locations and subdivision adopted in this study. The overall configuration of the model structure and the nodes–branches relation is shown in Figure 6. The model consists of 2 boundary nodes, 3 boundary branches, 37 internal nodes, and 46 branches.

The He/LOx drain was modelled by Nodes 1 to 23 and is representative of the duct used to discharge the mixture outside of the turbopump. The liquid oxygen comes from the LOx inlet conduit, the duct adopted in this test bench to simulate the injection of the oxidizer used as a coolant for the bearings. After passing through a kinetic slinger and a labyrinth seal, which aim to vapourize the cryogenic fluid to reduce the fluid pressure upstream of the seal drainage, the oxidizer flows into the He/LOx drain. The He is the buffer fluid and comes from the He inlet through a segmented seal. This duct is concentric to the drainage conduit, but is shifted by 90° and is modelled from Node 24 to Node 39. The necessity to simulate the He inlet duct arises from the need to estimate the wall temperature (from solid Nodes 1 to 8) to account for the influence of the heat exchanges between the mixture in the drain and the wall. The model included fluid-to-solid and solid-to-solid branches to take into account these heat fluxes. Moreover, as shown in Figure 6, to accurately estimate the pressure drops across branches (thus, the redistribution of flow rates), the relative local pressure drop was estimated for each branch, which is part of a junction.

3.2. Boundary Conditions

The boundary conditions for this model were derived from measured pressure and temperature data gathered during the test campaign of the DSP.

At each boundary branch, both the mass flow rate and the temperature (or quality) of the fluid entering the network were imposed. In the case of the oxygen boundary branch, the quality was not measured directly, but was calculated from the power supplied by the slinger to the fluid. Fluid Branches 1 and 2 represent the oxygen and He input to the drain, respectively, while Fluid Branch 3 depicts the He inlet input.

The outlet boundary conditions were imposed at the boundary nodes, where the pressure was defined. The two boundary nodes, 23 and 39, represent the output of the drain and the He duct.

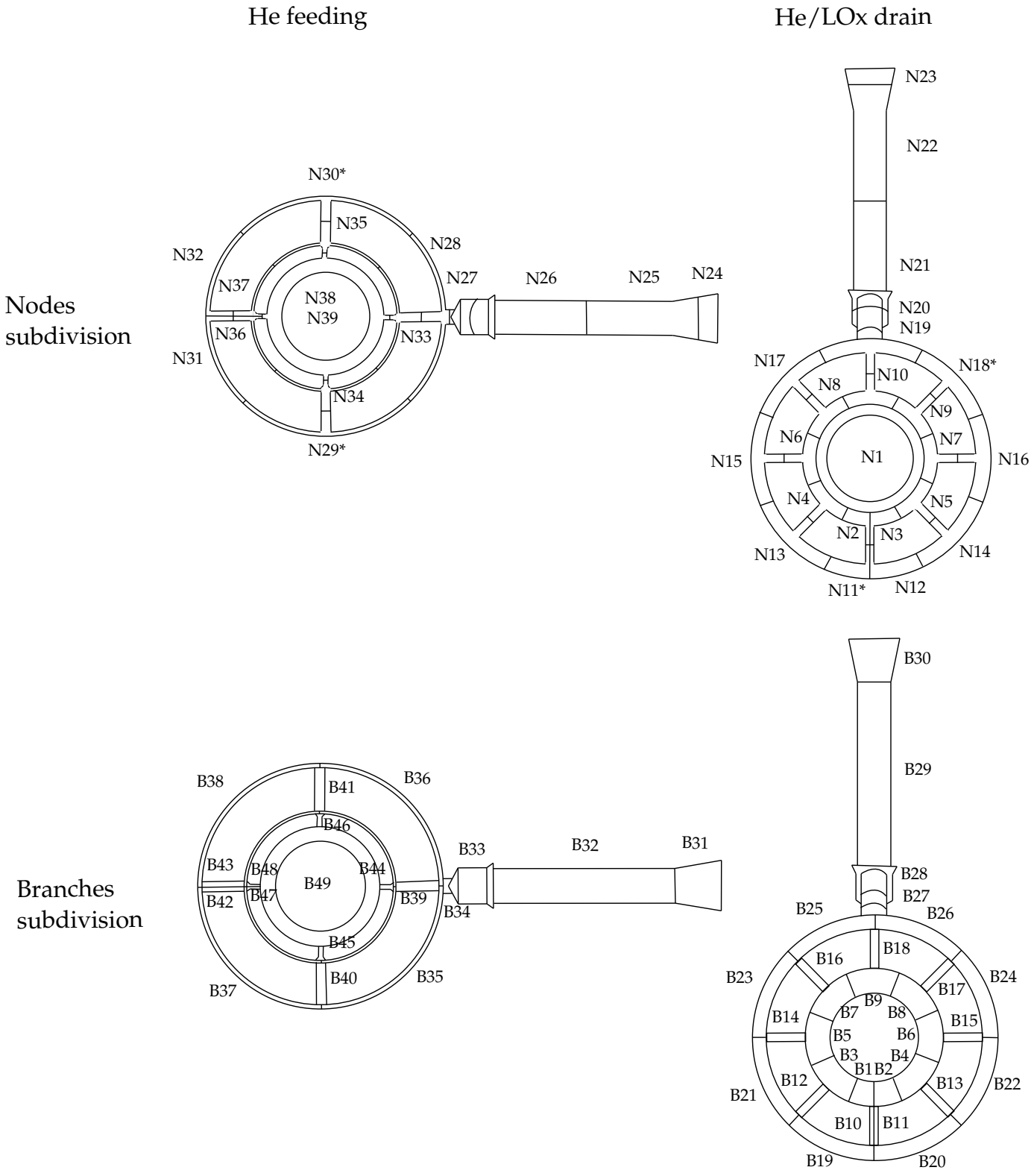


Figure 5. Node (**top**) and branch (**bottom**) subdivision of the He/LOx drain and He inlet of the Dynamic Seal Package test bench

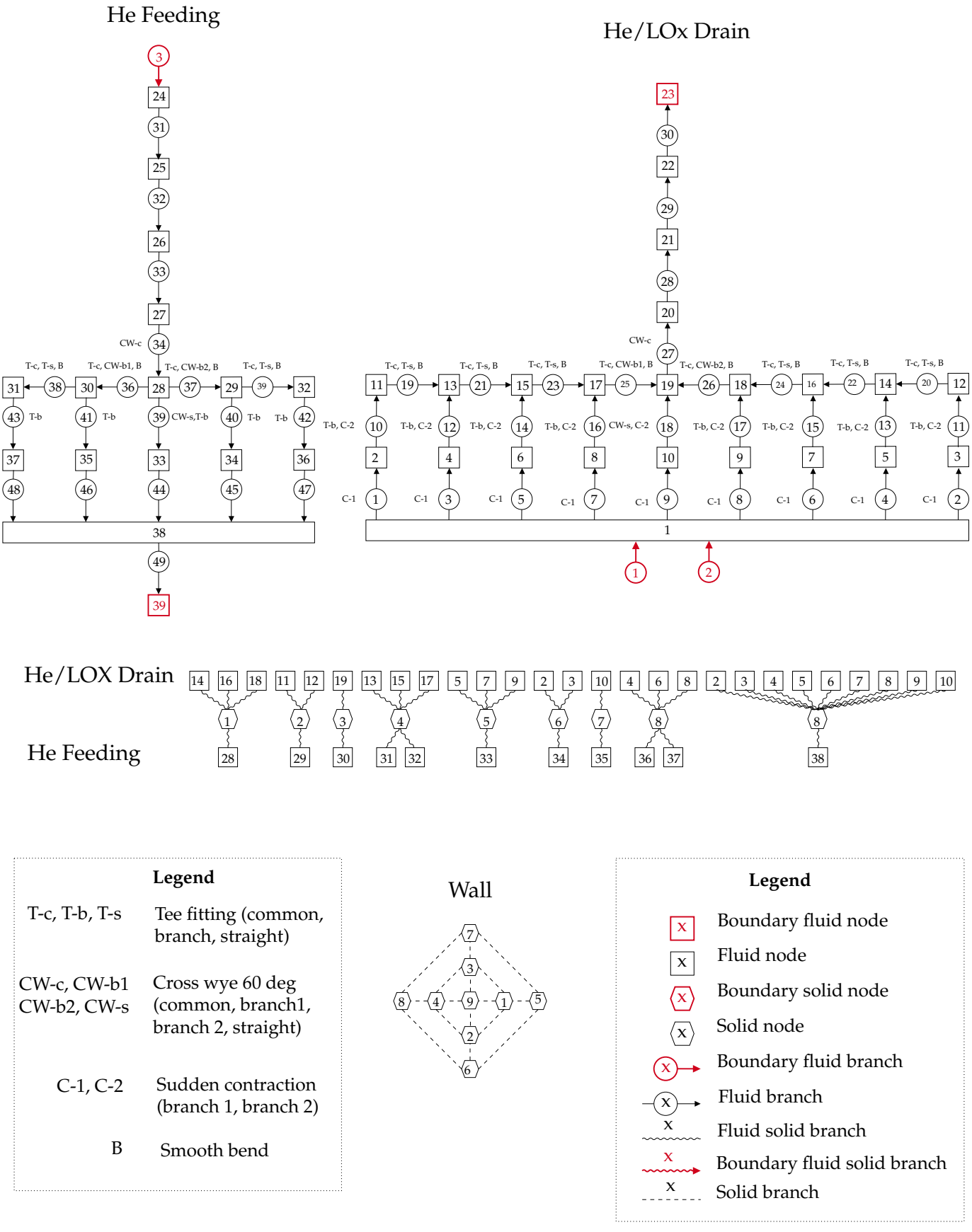


Figure 6. Model of the He/LOx drain and He inlet of the Dynamic Seal Package test bench.

Table 2 summarizes the boundary conditions for the different test cases under analysis. The difference between each test case is mainly the flow rate at the He inlet duct, which was progressively increased. A similar increase in the He flow rate also occurs in the drain duct, as half of the fluid flows through the segmented seal to the He/LOx drain and the other half to the GN2/He drain. Therefore, the analysis of these test cases made it possible to validate the numerical tool for a mixture characterized by a gradually increasing percentage of He.

Table 2. Boundary conditions for the different test cases under analysis, where B1, B2, and B3 are the boundary branches and N23 and N39 are the boundary nodes of the DSP model.

Boundary Conditions						
		Test Case 1	***Test Case 2***	***Test Case 3***	***Test Case 4***	***Test Case 5***
B1	x (−)	0.150	0.150	0.150	0.150	0.150
	p (MPa)	0.197	0.209	0.213	0.212	0.221
	$\dot{m}$ (g/s)	9.890	9.890	9.890	9.890	9.890
	Fluid			Oxygen		
B2	T (K)	270.95	274.930	276.83	278.27	279.60
	p (MPa)	1.151	1.291	1.393	1.504	1.600
	$\dot{m}$ (g/s)	1.590	1.850	2.060	2.250	2.460
	Fluid			Helium		
B3	T (K)	288.10	288.500	288.75	288.98	289.43
	p (MPa)	1.137	1.276	1.377	1.486	1.582
	$\dot{m}$ (g/s)	3.190	3.710	4.110	4.510	4.920
	Fluid			Helium		
N23	p (MPa)	0.197	0.209	0.213	0.212	0.221
N39	p (MPa)	1.151	1.291	1.393	1.504	1.600

4. Results

The steady-state results of modelling the He/LOx drain and He inlet of the Dynamic Seal Package test bench are presented in Figures 7–14. The boundary conditions used for this model are reported in the first test case of Table 2.

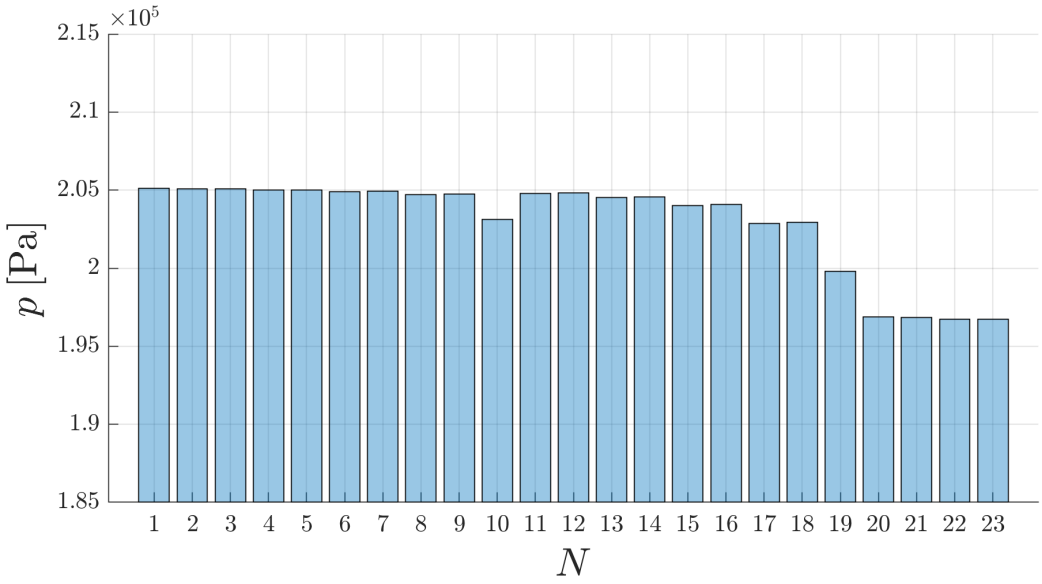


Figure 7. Pressure prediction at He/LOx drain conduit nodes.

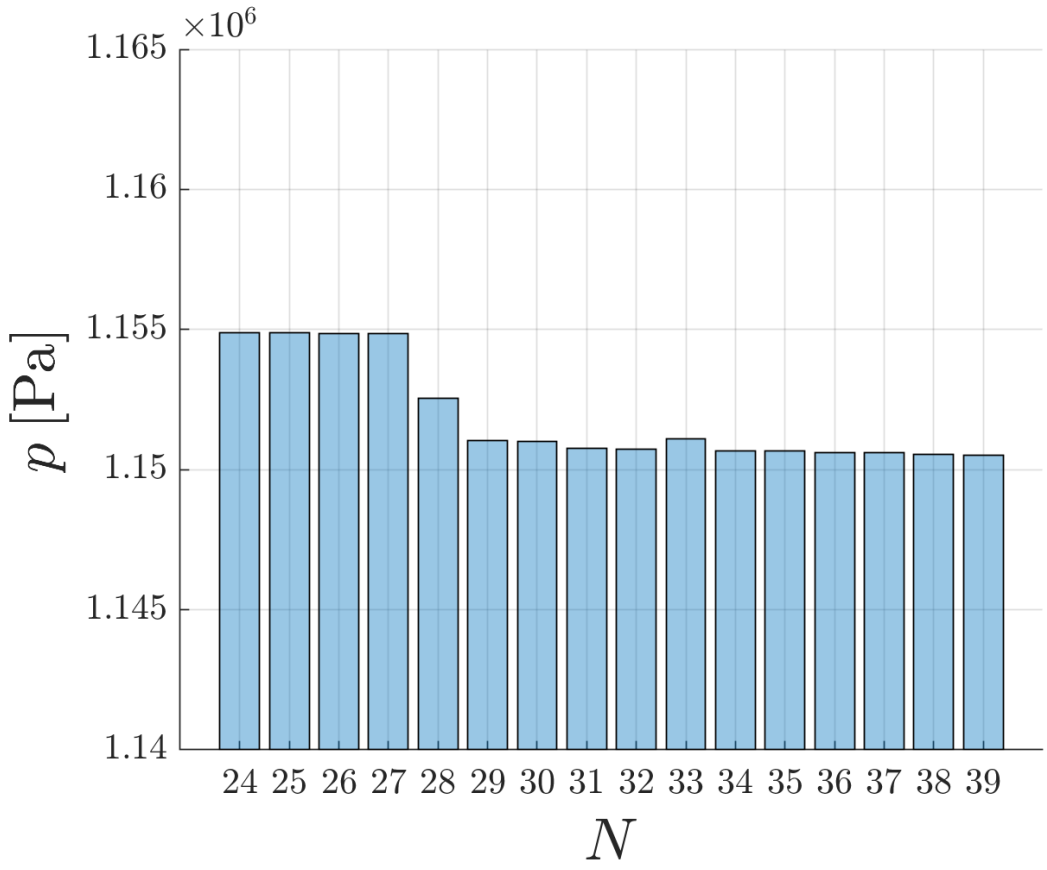


Figure 8. Pressure prediction at He inlet conduit nodes.

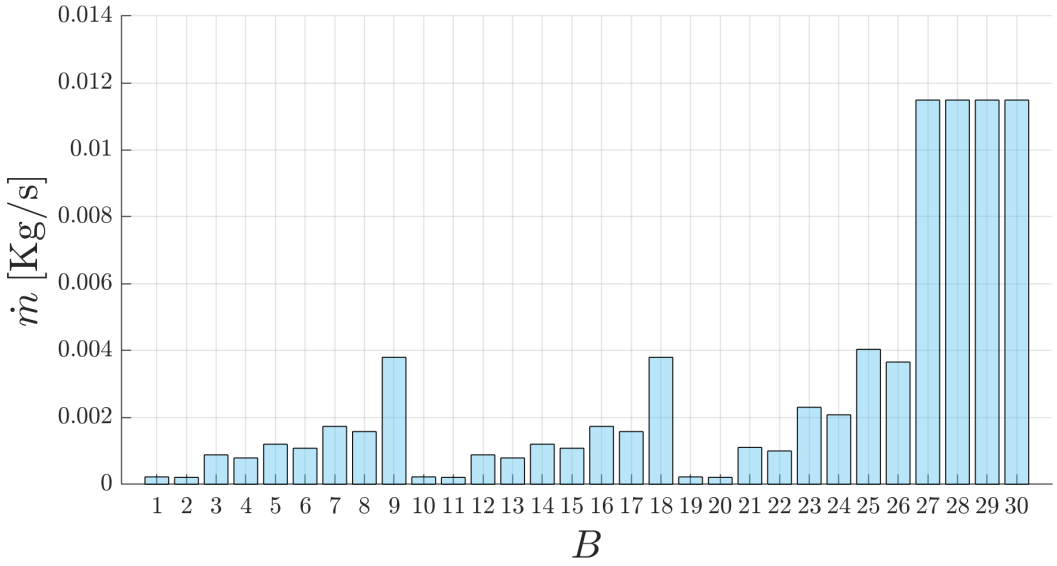


Figure 9. Mass flow rate prediction at He/LOx drain conduit branches.

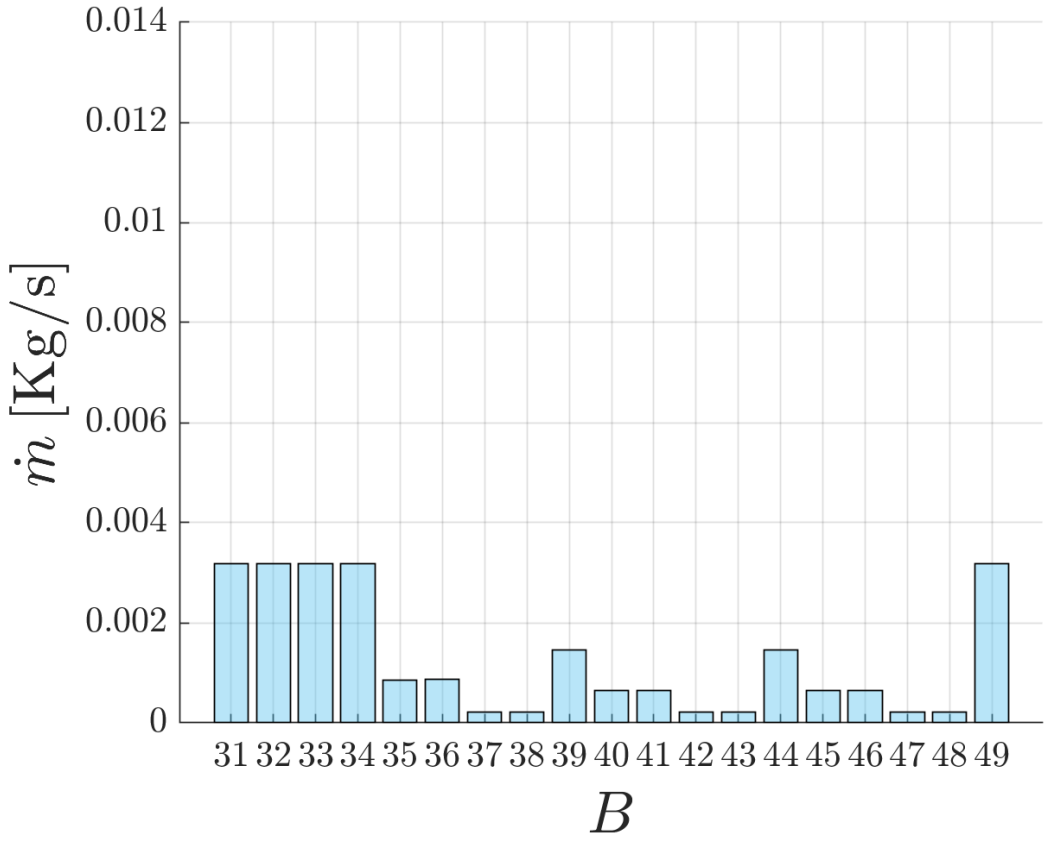


Figure 10. Mass flow rate prediction at He inlet conduit branches.

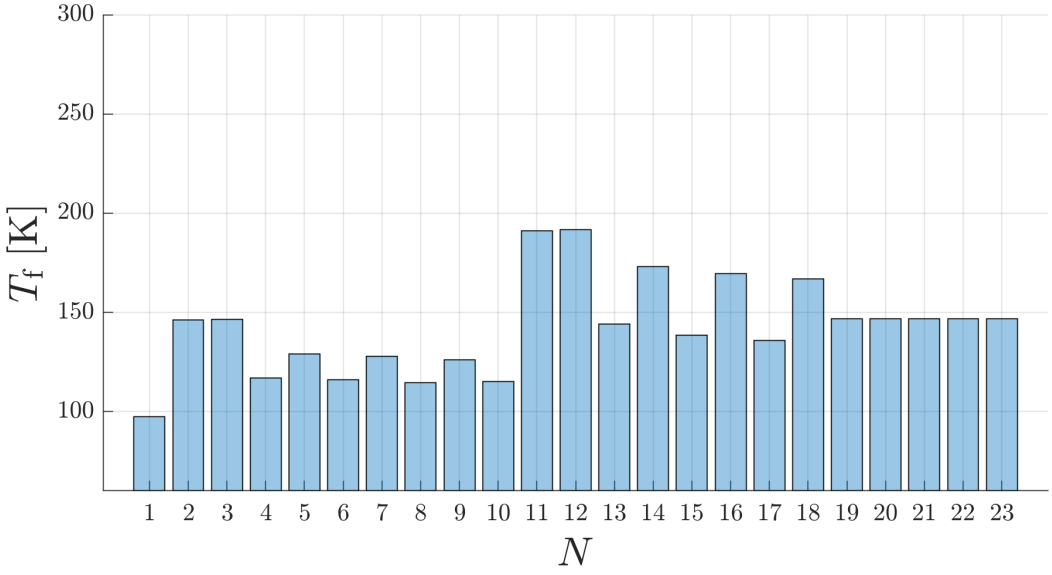


Figure 11. Temperature prediction at He/LOx drain conduit nodes.

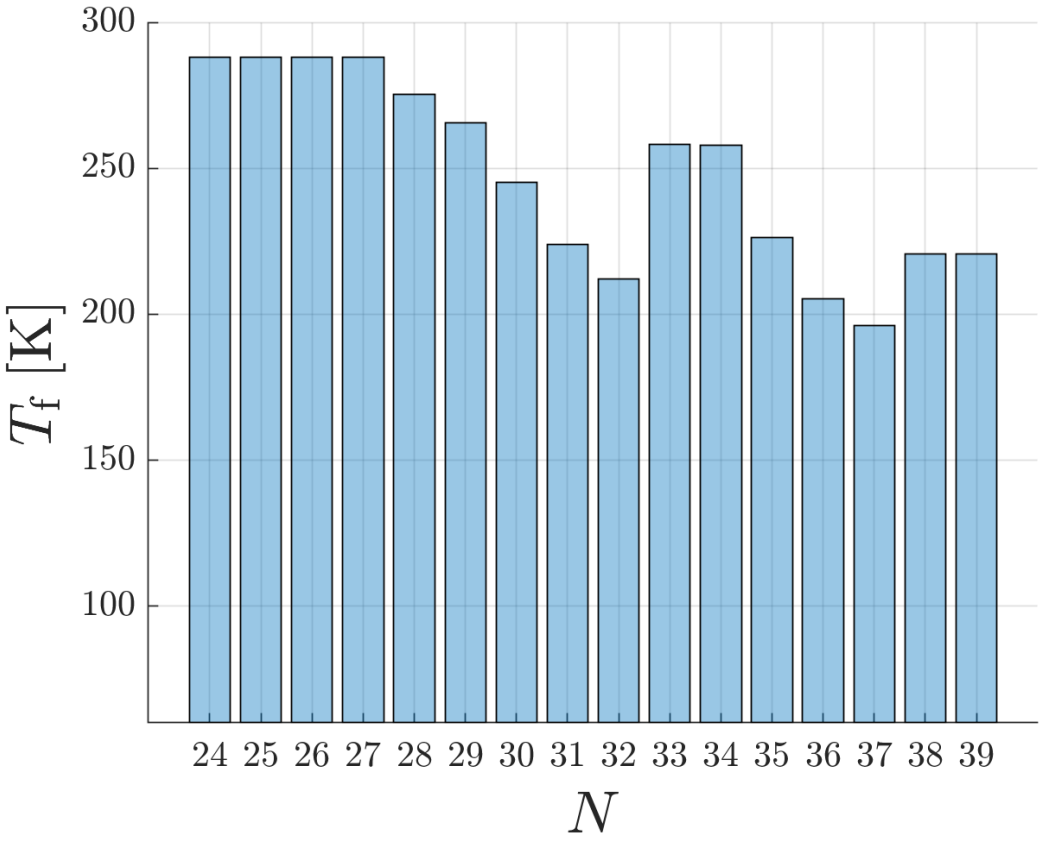


Figure 12. Temperature prediction at He inlet conduit nodes.

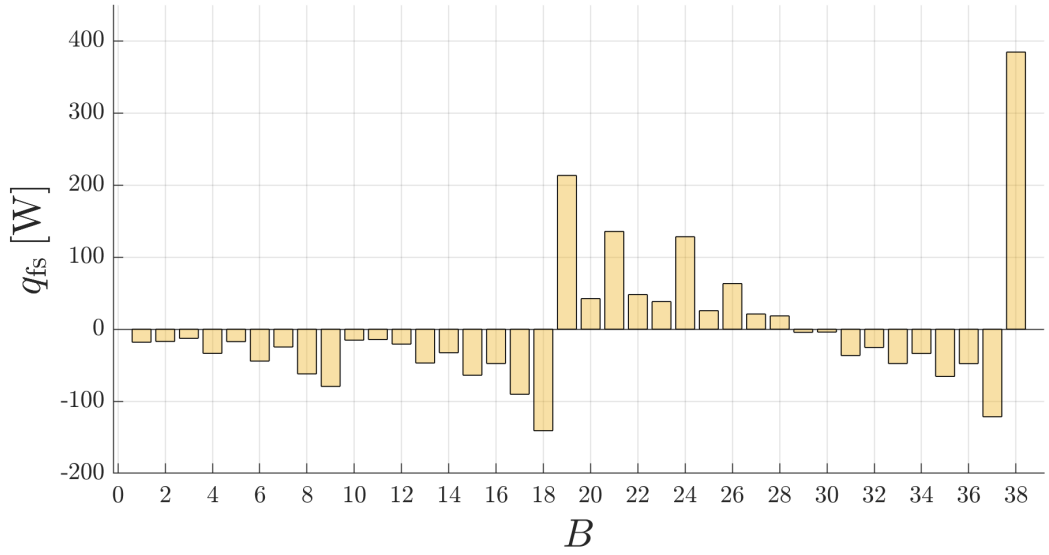


Figure 13. Heat flux prediction at branches between the fluid and solid nodes.

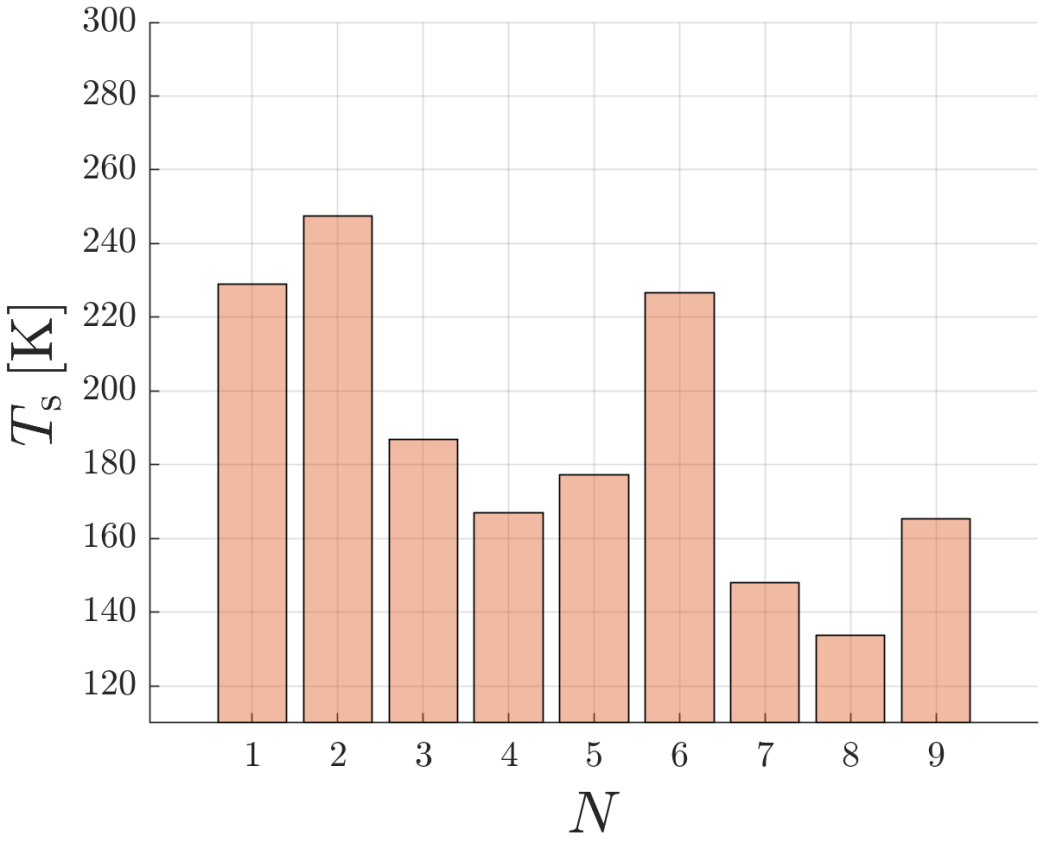


Figure 14. Temperature prediction at solid nodes between the He/LOx drain and He inlet conduit.

4.1. Discussion

The fluids involved in the analysis, LOx and He, mix in the drain conduit, generating a bi-component mixture, which is ejected from the turbopump, while pure He flows in the He inlet. A first check was performed comparing the He mass fraction (β_{He}) at the drainage outlet with the ratio of the inlet flow rates of the two fluids, $\beta_{\mathrm{He}} = 0.14$. This parameter is fundamental since it is used to determine the properties of the mixture on the basis of the ones of the pure oxygen and He.

Figures 7 and 8 show the pressure predictions in the two conduits. By analysing the trends, it is possible to assess a progressive pressure drop from the inlet of the ducts to the end. This loss is relatively small and is more significant in the drain conduit because of the higher flow rate and gravitational force.

The leading causes of these pressure losses are line and local losses due to junctions. Taking into account the pressure losses due to the junctions is necessary for modelling: the losses they generate, despite being relatively small, influence the redistribution of flows within radial ducts and, thus, the heat flux and fluid temperature in each duct. The flow rate governs the rate of energy transport into the control volume and, in addition, the forced convection heat transfer.

The results regarding the mass flow rates for the different branches are shown in Figures 9 and 10. Figure 9 shows that the flow coming from the labyrinth seal and the segmented seal is redistributed symmetrically with respect to the outlet duct. As expected, the ducts characterized by a longer flow path present a lower mass flow rate since they are less convenient because their paths have higher hydraulic resistance. All the fluid eventually flows through Branches 27–29. The same applies to the He duct, with the difference that there are fewer radial ducts and mass flow rates. In this case, the fluid flows from the inlet to the segmented seal.

Figures 11 and 12 show the predicted fluid temperature in the two conduits analysed. As seen from the two trends, the temperature of the He inlet is higher than the He/LOx drain temperature. Indeed, the He is injected at 288.1 K, while the temperature is significantly lower in the drain due to the two-phase oxygen at cryogenic temperatures from the labyrinth seal. By analysing the He inlet trend, it is possible to assess a temperature decrease from the inlet of the ducts to the end. This effect is due to heat exchange with the wall, which draws heat from the fluid. Indeed, the wall is at a lower temperature due to its proximity to the drain. In contrast, the He/LOx drain increases in temperature from the labyrinth seal to the outlet as it draws heat from the wall. Observing Figure 11, it can be assessed that the first node of the drainage has a temperature of 97.5 K, which corresponds to the saturation temperature at the pressure of Node 1; this implies that the oxygen is still in a two-phase condition at the segmented seal. However, the He injection at a high temperature caused the oxygen to rise in quality from $x_{ox} = 0.15$ to $x_{ox} = 0.86$. Furthermore, the presence of He, which has the characteristics of an inert gas, causes the mixture to have an overall gas fraction of $\psi = 0.88$. From the second node onward, oxygen is wholly vapourized (superheated steam).

In radial ducts, the temperature assumes different values. In particular, in the He inlet, the temperature decreases from the ducts radially opposite from the inlet. In contrast, the ducts radially farther from the outlet assume higher temperatures in the drain. The cause is attributed to the different redistributions in the different branches. Considering, for example, the drain, the long residence time of the fluid in the nodes farther from the outlet determines higher temperatures, despite the low values of the heat transfer coefficient due to the low mass flow rate. Similar reasoning can be applied to the He conduit. It is noted that, unlike in the distribution of flow rates, in this case, temperatures are not distributed symmetrically with respect to the central duct. This is due to the offset of 90° between the He inlet duct and the drain outlet duct. To confirm the previous phenomena, Figures 13 and 14 show the results of the heat flux and temperature of the solid nodes.

4.2. Model Validation

In order to validate the numerical tool, the fluid temperatures predicted by the numerical tool were compared with those measured in the He/LOx drainage and He inlet. Table 3 presents the comparison of the numerical predictions with the measured temperature data used for the validation.

Table 3. Temperatures of the He/LOx drain and He inlet from the computed (numerical tool) and experimental data.

		Results				
		Test Case 1	***Test Case 2***	***Test Case 3***	***Test Case 4***	***Test Case 5***
He/LOx Drain	T_A (K)	187.01	205.06	215.12	223.00	229.36
-	T_{11} (K)	191.04	199.61	205.14	209.62	213.97
Probe A	$E_{r_\%}$ (%)	**−2.15**	**2.65**	**4.63**	**5.99**	**6.70**
He/LOx Drain	T_B (K)	165.58	181.12	188.81	194.13	198.59
-	T_{18} (K)	166	178.18	185.18	191.03	196.83
Probe B	$E_{r_\%}$ (%)	**−0.81**	**1.61**	**1.92**	**1.59**	**0.88**
He Inlet	T_C (K)	270.95	274.93	276.83	278.27	279.60
-	T_{29} (K)	265.71	268.90	270.86	272.49	274.21
Probe C	$E_{r_\%}$ (%)	**1.93**	**2.19**	**2.15**	**2.07**	**1.92**
He Inlet	T_D (K)	250.53	257.52	260.62	263.06	265.31
-	T_{30} (K)	245.14	250.89	254.36	257.25	260.15
Probe D	$E_{r_\%}$ (%)	**2.14**	**2.57**	**2.40**	**2.20**	**1.94**

As previously mentioned, both pairs of probes used for validation are placed radially opposite in the outer crown, aligned with the drainage conduit. Therefore, the examined

nodes are 11 and 18 for the He/LOx drain and 29 and 30 for the He inlet. The validation of the tool was carried out by analysing the percentage error between the measurements and the prediction:

$$E_{r_{\%}} = \frac{T_{\text{predict}} - T_{\text{meas}}}{T_{\text{meas}}} 100 \quad (23)$$

As shown in Table 3, a good agreement of the predicted values with the experimental data (within 7%) can be observed.

5. Conclusions

This work described a 1D flow network solver developed to simulate two-phase multi-component flows inside cryogenic turbopumps used for liquid rocket engines. The flow network solver provides the capability to analyse very complex geometries, involving very narrow passages and fittings with mixing of different fluids. In particular:

1. A general-purpose finite volume procedure was implemented for solving the mass, momentum, and energy conservation equations of fluids and solids. The pressure drop and the convective single- and two-phase heat transfer, involved in the momentum and energy conservation equations, were calculated using empirical correlations.
2. The network solver was based on an extension of a classic 1D homogeneous model, originally developed for a pure substance, to the case of two-phase multi-component flow. Classical two-phase heat transfer and pressure drop models were adapted to multi-component flows by using an overall gas fraction.
3. The validation of the numerical tool was conducted by means of experimental data obtained for the secondary circuit of an oxidizer turbopump developed at Avio S.p.A.; the Dynamic Seal Package was considered, which includes leakage flow from the oxidizer pump discharge and mixing of the propellant with He.
4. The numerical predictions of fluid temperatures were compared with the measured data. In most cases, a very good agreement was observed between the measurements and predictions, with a maximum error lower than 7%, observed at the He/LOx drain.
5. The temperature discrepancies may be due to several factors. The assumed homogeneous model and the adopted correlations may be inadequate to capture the two-phase phenomena of a bi-component mixture. However, the use of a more sophisticated model, such as the drift–flux model or two-fluid model, would imply a larger computational cost without guaranteeing a considerable accuracy improvement due to the implicit uncertainties in predicting the interfacial interaction terms between the two phases.

Author Contributions: Conceptualization, M.A., C.B., G.C., F.M.M., L.M., and D.P; investigation, L.M. and F.M.M.; writing—original draft preparation, L.M. and F.M.M.; writing—review and editing, M.A., C.B., G.C., F.M.M., L.M., and D.P; supervision, M.A., C.B., G.C., F.M.M., and D.P.; project administration, D.P. and G.C. All authors have read and agreed to the published version of the manuscript.

Funding: This work was supported by Avio S.p.A. (Contract No. C119347–72/2021).

Institutional Review Board Statement: Not applicable.

Informed Consent Statement: Not applicable.

Data Availability Statement: Not applicable.

Conflicts of Interest: The authors declare no conflict of interest.

Nomenclature

Symbols

A	Branch area (m^2)
c_{p}	Specific heat $(\mathrm{J}/(\mathrm{kg\,K}))$
D_{h}	Hydraulic diameter (m)

$E_{r_{\%}}$	Percentage error (%)
f	Darcy friction factor
g	Gravity acceleration (m/s)
G	Mass flux (kg/(m^2 s))
h	Enthalpy (J/kg), heat transfer coefficient (W/(m^2 K))
h_{lv}	Enthalpy of evaporation (J/kg)
h'_{lv}	Equivalent enthalpy of evaporation (J/kg)
k	Thermal conductibility (W/(m K))
K_{rot}	Rotation factor between fluid and surrounding surface (-)
L	Branch length (m)
m	Mass (kg)
$\dot{m}$	Mass flow rate (kg/s)
n	Number of elements in the network (-)
n_{fb}	Number of fluid-to-fluid branches in the network (-)
n_{fn}	Number of fluid nodes in the network (-)
n_{fn_i}	Fluid nodes adjacent to node i (-)
n_{fsb}	Number of fluid-to-solid branches in the network (-)
n_{ifn}	Number of internal fluid nodes in the network (-)
n_{s}	Number of species in the network (-)
n_{sb}	Number of solid-to-solid branches in the network (-)
n_{sn}	Number of solid nodes in the network (-)
n_{sn_i}	Solid nodes adjacent to node i (-)
p	Pressure (Pa)
Pr	Prandtl number (-)
$\dot{Q}$	Heat flux (W)
$\dot{q}$	Heat flux (W/m^2)
Re	Reynolds number (-)
T	Temperature (K)
t	Time (s)
u	Velocity (m/s)
V	Volume (m^3)
x	Quality (-)
Greeks	
β	Mass fraction (-)
δ	Solid node distance (m)
Δt	Time interval between time steps (s)
ε	Absolute roughness (m)
θ	Branch inclination angle respect to gravity (rad)
μ	Viscosity (Pa · s)
ρ	Density (kg/m^3)
σ	Surface tension (N/m)
χ	Molar fraction (-)
ψ	Overall gas fraction (-)
ω	Angular velocity (rad/s)
Subscripts and superscripts	
annular	Annular flow
CHF	Critical heat flux
disp	Dispersed flow
f	Friction, fluid node variable (or unspecified)
ff	Fluid-to-fluid branch variable (or unspecified)
fs	Fluid-to-solid branch variable
i	Node index
ij	Branch index from node i to node j
j	Node index adjacent to cell i
ji	Branch index from node j to node i
k	Specie, Local
l	Saturated liquid, line
MHF	Minimum heat flux

s	Solid node variable
sat	Saturation condition
sp	Single-phase flow
sf	Solid-to-fluid branch variable
ss	solid-to-solid branch variable
tp	Two-phase flow
t	Time step
$t + \Delta t$	New time step
u	Upstream branch
v	Saturated vapour
Acronyms	
DSP	Dynamic Seal Package
He	Helium
LOx	Liquid oxygen
GN2	Gaseous nitrogen

References

1. Sutton, G.P.; Biblarz, O. *Rocket Propulsion Elements*; Wiley: Hoboken, NJ, USA, 2017.
2. Meyer, M.L.; Chato, D.J.; Plachta, D.W.; Zimmerli, G.A.; Barsi, S.J.; Van Dresar, N.T.; Moder, J.P. Mastering cryogenic propellants. *J. Aerosp. Eng.* **2013**, *26*, 343–351.
3. Lo, R.E. Modular Dissected Cryogenic Solid-Rocket Propellant Grains. *Acta Astronaut.* **2002**, *51*, 683–691.
4. Deng, B.; Yang, S.; Xie, X.; Wang, Y.; Pan, W.; Li, Q.; Gong, L. Thermal performance assessment of cryogenic transfer line with support and multilayer insulation for cryogenic fluid. *Appl. Energy* **2019**, *250*, 895–903.
5. Darr, S.; Dong, J.; Glikin, N.; Hartwig, J.; Majumdar, A.; Leclair, A.; Chung, J. The effect of reduced gravity on cryogenic nitrogen boiling and pipe chilldown. *NPJ Microgravity* **2016**, *2*, 16033.
6. Kumar, S.; Kwon, H.T.; Choi, K.H.; Lim, W.; Cho, J.H.; Tak, K.; Moon, I. LNG: An eco-friendly cryogenic fuel for sustainable development. *Appl. Energy* **2011**, *88*, 4264–4273.
7. Hartwig, J.; Darr, S.; Asencio, A. Assessment of existing two phase heat transfer coefficient and critical heat flux correlations for cryogenic flow boiling in pipe quenching experiments. *Int. J. Heat Mass Transf.* **2016**, *93*, 441–463.
8. Ishii, M.; Hibiki, T. *Thermo-Fluid Dynamics of Two-Phase Flow*; Springer: Berlin/Heidelberg, Germany, 2006.
9. Liao, Z. Single Molecule Study of Photoconversion and Spectral Heterogeneities of Fluorophores. Ph.D. Thesis, Faculty of Science, University of Copenhagen, Kobenhavn, Denmark, 2014.
10. Yuan, K.; Ji, Y.; Chung, J. Numerical modeling of cryogenic chilldown process in terrestrial gravity and microgravity. *Int. J. Heat Fluid Flow* **2009**, *30*, 44–53.
11. Wang, J.; Li, Y.; Wang, L.; Zhao, Y.; Ishii, M. Thermal prediction of transient two-phase flow in cryogenic transportation based on drift–flux model. *Int. J. Heat Mass Transf.* **2021**, *177*, 121512.
12. Li, C.; Li, Y.; Cheng, Y.; Chen, E.; Liu, Z.; Wang, J. Transient characteristics and performances of passive recirculation system for liquid rocket engine precooling. *Appl. Therm. Eng.* **2019**, *149*, 41–53.
13. Hooser, K.V.; Bailey, J.; Majumdar, A. Numerical prediction of transient axial thrust and internal flows in a rocket engine turbopump. In Proceedings of the 35th Joint Propulsion Conference and Exhibit, Los Angeles, CA, USA, 20–24 June 1999.
14. Majumdar, A. Generalized Fluid System Simulation Program, Version 6.0, 2013. Available online: https://ntrs.nasa.gov/api/citations/20140003178/downloads/20140003178.pdf (accessed on 1 January 2022).
15. Hu, H.; Chung, J.N.; Amber, S.H. An experimental study on flow patterns and heat transfer characteristics during cryogenic chilldown in a vertical pipe. *Cryogenics* **2012**, *52*, 268–277.
16. Johnson, J.; Shine, S. Transient cryogenic chill down process in horizontal and inclined pipes. *Cryogenics* **2015**, *71*, 7–17.
17. Darr, S.; Hu, H.; Glikin, N.; Hartwig, J.; Majumdar, A.; Leclair, A.; Chung, J. An experimental study on terrestrial cryogenic tube chilldown II. Effect of flow direction with respect to gravity and new correlation set. *Int. J. Heat Mass Transf.* **2016**, *103*, 1243–1260.
18. Hartwig, J.; Styborski, J.; McQuillen, J.; Rame, E.; Chung, J. Liquid hydrogen line chilldown experiments at high Reynolds Numbers. Optimal chilldown methods. *Int. J. Heat Mass Transf.* **2019**, *137*, 703–713.
19. Jin, L.; Park, C.; Cho, H.; Lee, C.; Jeong, S. Experimental investigation on chill-down process of cryogenic flow line. *Cryogenics* **2016**, *79*, 96–105.
20. Jin, L.; Lee, J.; Jeong, S. Investigation on heat transfer in line chill-down process with various cryogenic fluids. *Int. J. Heat Mass Transf.* **2020**, *150*, 119204.
21. Shaeffer, R.; Hu, H.; Chung, J. An experimental study on liquid nitrogen pipe chilldown and heat transfer with pulse flows. *Int. J. Heat Mass Transf.* **2013**, *67*, 955–966.
22. Hartwig, J.W.; Rame, E.; McQuillen, J. Pulse chilldown tests of a tank-to-tank liquid hydrogen propellant transfer line. In Proceedings of the 54th AIAA Aerospace Sciences Meeting, San Diego, CA, USA, 4–8 January 2016; p. 2186.
23. Hu, H.; Wijeratne, T.K.; Chung, J.N. Two-Phase Flow and Heat Transfer During Chilldown of a Simulated Flexible Metal Hose Using Liquid Nitrogen. *J. Low Temp. Phys.* **2013**, *174*, 247–268.

24. Chung, J.; Darr, S.; Dong, J.; Wang, H.; Hartwig, J. Heat transfer enhancement in cryogenic quenching process. *Int. J. Therm. Sci.* **2020**, *147*, 106117.
25. Kim, S.M.; Mudawar, I. Review of databases and predictive methods for heat transfer in condensing and boiling mini/micro-channel flows. *Int. J. Heat Mass Transf.* **2014**, *77*, 627–652.
26. Mazzei, L.; Marin, F.M.; Bianchini, C.; Soghe, R.D.; Bertani, C.; Pastrone, D.; Angelucci, M.; Caggiano, G.; de Beer, M. Analysis of a Stator-Rotor-Stator Spinning Disk Reactor in Single-Phase and Two-Phase Boiling Conditions Using a Thermo-Fluid Flow Network and CFD. *Fluids* **2022**, *7*, 42.
27. Dittus, F.; Boelter, L. Heat transfer in automobile radiators of the tubular type. *Int. Commun. Heat Mass Transf.* **1985**, *12*, 3–22.
28. Wang, J.; Li, Y.; Wang, L.; Zhu, K.; Xie, F.; Li, C. Transient modeling of cryogenic two-phase flow boiling during chill-down process. *Appl. Therm. Eng.g* **2018**, *143*, 461–471.
29. Hill, W.S.; Rohsenow, W.M. *Dryout Droplet Distribution and Disperse Flow Film Boiling*; Technical Report 85694-105; Massachusetts Institute of Technology: Cambridge, MA, USA, 1982.
30. Bromley, L.A. *Heat Transfer in Stable Film Boiling*; US Atomic Energy Commission, Technical Information Division: Washington, DC, USA, 1949; Volume 2295.
31. Zuber, N.; Fried, E. Two-phase flow and boiling heat transfer to cryogenic liquids. *ARS J.* **1962**, *32*, 1332–1340.
32. Darr, S.R.; Dong, J.; Glikin, N.; Hartwig, J.W.; Chung, J.N. Rewet Temperature Correlations for Liquid Nitrogen Boiling Pipe Flows Across Varying Flow Conditions and Orientations. *J. Therm. Sci. Eng. Appl.* **2019**, *11*, 051008. https://doi.org/10.1115/1.4042857.
33. Kalinin, E.K.; Yarkho, S.A.; Berlin, I.I.; Kochelaev, Y.S.; Kostyuk, V.V. Investigation of the boiling crisis and heat transfer in dispersed-film boiling of liquids in channels. *Heat Transfer. Soviet Research* **1987**, *19*, 1.
34. Colebrook, C.F. Turbulent Flow in Pipes, With Particular Reference to the Transition Region Between the Smooth and Rough Pipe Laws. *J. Inst. Civ. Eng.* **1939**, *11*, 133–156.
35. Qi, S.; Zhang, P.; Wang, R.; Xu, L. Single-phase pressure drop and heat transfer characteristics of turbulent liquid nitrogen flow in micro-tubes. *Int. J. Heat Mass Transf.* **2007**, *50*, 1993–2001.
36. Zhang, P. Flow and Heat Transfer Characteristics of Liquid Nitrogen in Mini-/Microchannels. *Heat Transf. Eng.* **2013**, *34*, 204–212.
37. Chen, X.; Hou, Y.; Chen, S.; Liu, X.; Zhong, X. Characteristics of frictional pressure drop of two-phase nitrogen flow in horizontal smooth mini channels in diabatic/adiabatic conditions. *Appl. Therm. Eng.* **2019**, *162*, 114312.
38. Yun, J.H.; Jeong, J.H. A Review of Prediction Methods for Two-Phase Pressure Loss in Mini/Micro-Channels. *Int. J.-Air-Cond. Refrig.* **2016**, *24*, 1630002.
39. Qi, S.; Zhang, P.; Wang, R.; Xu, L. Flow boiling of liquid nitrogen in micro-tubes: Part I—The onset of nucleate boiling, two-phase flow instability and two-phase flow pressure drop. *Int. J. Heat Mass Transf.* **2007**, *50*, 4999–5016.
40. Chen, G.F.; Gong, M.; Wang, S.; Wu, J.F.; Zou, X.; Sun, Z. Two-phase frictional pressure drop of methane in a horizontal tube: Experimental investigation and comparison with correlations. *AIP Conf. Proc.* **2012**, *1434*, 1051.
41. Chen, D.; Shi, Y. Study on two-phase pressure drop of LNG during flow boiling in a 8 mm horizontal smooth tube. *Exp. Therm. Fluid Sci.* **2014**, *57*, 235–241.
42. Friedel, L. Improved Friction Pressure Drop Correlation for Horizontal and Vertical Two-Phase Pipe Flow. In Proceedings of the European-American-Japanese Two-Phase Flow Group Meeting, Ispra, Italy, 5–8 June 1979.
43. Müller-Steinhagen, H.; Heck, K. A simple friction pressure drop correlation for two-phase flow in pipes. *Chem. Eng. Process. Process. Intensif.* **1986**, *20*, 297–308.
44. Idelchik, I.E. *Handbook of Hydraulic Resistance*; CRC Press: Boca Raton, FL, USA, 1994.
45. Bell, I.H.; Wronski, J.; Quoilin, S.; Lemort, V. Pure and Pseudo-pure Fluid Thermophysical Property Evaluation and the Open-Source Thermophysical Property Library CoolProp. *Ind. Eng. Chem. Res.* **2014**, *53*, 2498–2508.
46. Galántai, A. The theory of Newton's method. *J. Comput. Appl. Math.* **2000**, *124*, 25–44.
47. Broyden, C.G. A class of methods for solving nonlinear simultaneous equations. *Math. Comput.* **1965**, *19*, 577–593.